



# Enhancing ammonia catalytic production over spatially confined cobalt molybdenum nitride nanoparticles in SBA-15

Amanda Sfeir<sup>a</sup>, Camila A. Teles<sup>a</sup>, Carmen Ciotonea<sup>a,b</sup>, G.N. Manjunatha Reddy<sup>a</sup>,  
Maya Marinova<sup>c</sup>, Jérémy Dhainaut<sup>a</sup>, Axel Löfberg<sup>a</sup>, Jean-Philippe Dacquin<sup>a</sup>,  
Sébastien Royer<sup>a,\*</sup>, Said Laassiri<sup>d,\*</sup>

<sup>a</sup> Université de Lille, CNRS, ENSCL, Centrale Lille, Univ. Artois, UMR 8181-UCSC-Unité de Catalyse et de Chimie du Solide, F-59000 Lille, France

<sup>b</sup> Univ. Littoral Côte d'Opale, UR 4492, UCEIV, Unité de Chimie Environnementale et Interactions sur le Vivant, SFR Condorcet FR CNRS 3417, F-59140 Dunkerque, France

<sup>c</sup> Université de Lille, CNRS, INRA, Centrale Lille, Université Artois, FR 2638 – IMEC – Institut Michel-Eugène Chevreul, 59000 Lille, France

<sup>d</sup> Chemical & Biochemical Sciences, Green Process Engineering (CBS), Mohammed VI Polytechnic University, UM6P, 43150 Benguerir, Morocco

## ARTICLE INFO

### Keywords:

Ammonia synthesis  
Nitrides  
Confined nanoparticles  
SBA-15

## ABSTRACT

Ternary  $\text{Co}_3\text{Mo}_3\text{N}$  nitrides are reported to exhibit high catalytic activity in ammonia synthesis. However, synthesis of ternary nitrides requires thermal treatments at elevated temperatures and reactive atmospheres that lead to unavoidable surface reduction ( $\sim 10 \text{ m}^2 \text{ g}^{-1}$ ). In this work, we have developed a novel approach to improve the catalytic activity of  $\text{Co}_3\text{Mo}_3\text{N}$  through its dispersion into a high surface area silica-based support (SBA-15). During ammonolysis and ammonia synthesis conditions reaction, SBA-15 demonstrated good thermal and chemical stability maintaining an ordered porous structure and high surface area ( $> 500 \text{ m}^2 \text{ g}^{-1}$ ). For application in ammonia synthesis, SBA-15 supported cobalt molybdenum catalysts with different metal loading (10, 20 and 30 wt%) were prepared by a modified impregnation-infiltration protocol and their catalytic activity studied. The dispersion of CoMo nitride nanoparticles into SBA-15 structures resulted in the improvement of their structural and textural properties of nitrides as evidenced by XRD analysis, STEM-EDS, and  $\text{N}_2$  physisorption (e.g. 10-CoMo-N/SBA-15:  $348 \text{ m}^2 \text{ g}^{-1}$ ). Nevertheless, the surface composition of CoMo-N/SBA-15 catalysts was found to be similar to the non-supported  $\text{Co}_3\text{Mo}_3\text{N}$ . Furthermore, supported CoMo-N/SBA-15 displayed enhanced catalytic activity in ammonia synthesis (1714, 1429 and  $810 \mu\text{mol g}_{\text{active}}^{-1} \text{ phase h}^{-1}$  corresponding to the CoMo oxide loadings of 10, 20, 30 wt% respectively) that outperform the classical  $\text{Co}_3\text{Mo}_3\text{N}$  catalyst ( $259 \mu\text{mol g}_{\text{catalyst}}^{-1} \text{ h}^{-1}$ ). The results reported in this work highlights a novel approach for the design of nitride-based catalysts with superior catalytic properties in ammonia synthesis.

## 1. Introduction

To compensate the natural variation of power derived from natural resources, the development of smart grid capable of cooperative electricity generation (mix of energy resources) and offering a range of energy storage possibilities (short-, mid- and long- term energy storage) is of high importance for large-scale renewable energy production. Among the energy storage systems, Power to X (P2X) is expected to play a major role in long-term, large scale energy storage (days to months). Within the multiple candidates for P2X, ammonia possesses suitable characteristics to be considered as green, safe and sustainable energy carrier, such as high hydrogen gravimetric content (17.6 wt%), high energy

density ( $5.2 \text{ kWh kg}^{-1}$ ) based on the low heat value (LHV), facile liquefaction and low flammability [1]. More importantly, there is an existing infrastructure for the safe and cost-effective ammonia transportation and distribution worldwide which alas is not the case for hydrogen [2].

The implementation of large-scale power to green ammonia, in the energy landscape is limited by the development of novel and efficient processes for cost-effective green ammonia production. Currently, large-scale ammonia production is achieved through the industrial Haber-Bosch process (H-B) in which highly purified  $\text{N}_2$  and  $\text{H}_2$  react over a promoted iron-based catalyst under high pressure (up to 200 bar) and temperature varying between 400 and  $500^\circ\text{C}$  [3,4]. While it sustains a

\* Corresponding authors.

E-mail addresses: [sebastien.royer@univ-lille.fr](mailto:sebastien.royer@univ-lille.fr) (S. Royer), [said.laassiri@um6p.ma](mailto:said.laassiri@um6p.ma) (S. Laassiri).

<https://doi.org/10.1016/j.apcatb.2022.122319>

Received 1 August 2022; Received in revised form 9 December 2022; Accepted 19 December 2022

Available online 21 December 2022

0926-3373/© 2022 Elsevier B.V. All rights reserved.

significant proportion of the global population through providing affordable nitrogen-based fertilizers, the process is highly energy demanding. The H-B process is estimated to consume  $\sim 1\text{--}2\%$  of the world's annual energy production of which 15% of energy requirements are solely consumed by high-pressure operations [5]. Currently, a considerable effort is centred upon the development of highly active catalysts capable of accelerating ammonia synthesis reaction at milder conditions and preferably at pressures aligned to those of green hydrogen produced by water electrolysis ( $10 \sim 80$  bar) [6]. From a thermodynamic point of view, producing ammonia at pressures lower than those used in the H-B process is possible provided that the reaction is conducted under low temperatures [7]. Thus, the development of novel generation of catalysts capable of operating at milder conditions is an important milestone in the deployment of large-scale Power to Ammonia process for energy storage.

Among the catalysts studied for ammonia synthesis, noble-metal based materials (e.g. Ru/graphite and  $\text{CoRe}_4$ ) have been reported to display superior catalytic activity when compared to the industrial catalyst. [8] However, considering the cost of noble metals and their scarcity, there is much interest in the development of non-noble metal-based catalysts for ammonia generation. One of the most active catalysts reported in the literature is  $\text{Co}_3\text{Mo}_3\text{N}$  ternary nitride (ammonia synthesis rate of  $330\text{--}652 \mu\text{mol h}^{-1} \text{g}^{-1}$  at  $400^\circ\text{C}$  and atmospheric pressure) [9] with catalytic performance at high pressure exceeding the industrial H-B doubly promoted iron-based catalyst [10]. Hence, there is a legitimate interest in further increasing the catalytic activity of  $\text{Co}_3\text{Mo}_3\text{N}$ . In the earlier studies, the high catalytic activity of  $\text{Co}_3\text{Mo}_3\text{N}$  was attributed to the presence of both Co and Mo in the termination plane (111) resulting in an optimal N-binding energy [11]. Initially, the role of nitrogen was believed to be limited to creating the right termination plane containing both Co and Mo. However, recent studies shed the light on the mobility and reactivity of nitrogen in  $\text{Co}_3\text{Mo}_3\text{N}$  via  $^{15}\text{N}/^{14}\text{N}$  isotopic exchange studies and by DFT calculation pinpointing the potential role of the lattice nitrogen in ammonia synthesis via routes akin to the Mars-van Krevelen (MvK) mechanism [12–14]. Recently, the mobility and reactivity of lattice nitrogen, in binary and ternary nitrides, towards hydrogen has been the focus of several research activities [15–17]. The capacity of some metal nitrides (e.g.  $\text{Ta}_3\text{N}_5$ ,  $0\text{-Mn}_6\text{N}_{5+x}$ ,  $\text{AlN}$ ,  $\text{Li}_3\text{N}$ ) to act as a source of pre-activated nitrogen has been of high interest especially for the development of ammonia production by chemical looping. In this approach, the lattice nitrogen reacts first with hydrogen to produce ammonia. The depleted nitrogen transfer material is regenerated upon reaction with atmospheric  $\text{N}_2$  in a second step. Related to this concept, the nitrogen mobility and reactivity of several nitrogen transfer materials have been explored including  $\text{Mn}_6\text{N}_{5+x}$ ,  $\text{AlN}$  and  $\text{Li}_3\text{N}$  [18–20]. In several cases, the activity of catalysts operating through mechanism akin to MvK was found to be strongly dependent upon: (i) structural and textural properties (e.g. exposed surface and crystal size) (ii) chemical composition and/or (iii) a combination of both [21,22]. Unfortunately, the preparation of  $\text{Co}_3\text{Mo}_3\text{N}$  requires at least one calcination step at  $550^\circ\text{C}$  to form the oxide precursor ( $\text{CoMoO}_4$ ), once the oxide is obtained, the nitride phase is formed by an ammonolysis step, under a flow of pure ammonia, at  $750^\circ\text{C}$ . The different thermal treatments result in crystal growth and unavoidable surface reduction ( $\sim 10 \text{ m}^2 \text{g}^{-1}$ ). As such, there is a high interest in the development of novel approaches for the preparation of divided nitride phases, displaying high surface area and retaining small nanoparticle size. At the nanoscale level, the catalytic activity is expected to increase due to the increase of the surface to volume (A/V) atom ratio, which increases both available surface area and active site density for catalytic reactions. Furthermore, ammonia synthesis reaction has been evidenced to be structure-sensitive [23,24]. Tsuji et al. demonstrated that the formation of bimetallic Co-Mo nanoparticles supported on  $\text{CeO}_2$ , prepared by NaNaph driven reduction, resulted in higher catalytic activity in ammonia synthesis [25]. The authors concluded that the formation of nitrogen vacancies occurs more easily on Co-Mo nanoparticles when

supported over ceria than for bulk  $\text{Co}_3\text{Mo}_3\text{N}$ . Such vacancies formation can explain the better performances reported for Co-Mo/ $\text{CeO}_2$  catalyst. Thus, enhancing the surface concentration on steps and defects through the dispersion of active nanoparticle nitrides is a tantalizing approach for improving the catalytic activity of nitride materials.

In this work, we implemented a novel strategy to improve the catalytic activity of  $\text{Co}_3\text{Mo}_3\text{N}$  by confining the active phase within the mesopore of SBA-15 silica. SBA-15 was utilized as a suitable support due to its: (i) high surface area; (ii) highly ordered and uniform mesopores; and (iii) good thermal stability. The catalysts were evaluated in the ammonia synthesis reaction conducted at  $400^\circ\text{C}$  and under atmospheric pressure. The effect of the textural and structural properties on the physicochemical properties and catalytic activity was investigated through an extensive characterization study. The positive effect of confining the active phase within the porosity of SBA-15 was demonstrated in ammonia synthesis.

## 2. Experimental

### 2.1. Catalyst preparation

**Chemicals.** All chemicals needed for the preparation of mesoporous SBA-15 support and CoMo-N/SBA-15 materials were used as purchased without further purification: tetraethylorthosilicate ( $\text{Si}(\text{OC}_2\text{H}_5)_4$ ), TEOS, 98 wt%, Sigma-Aldrich), non-ionic triblock co-polymer Pluronic P123 (poly(ethylene glycol)-*block*-poly(propylene glycol)-*block*-poly(ethylene glycol), average MW  $\sim 5800$ , Sigma-Aldrich), cobalt nitrate hexahydrate ( $\text{Co}(\text{NO}_3)_2 \cdot 6 \text{H}_2\text{O}$ , 98 wt%, Sigma Aldrich) and ammonium paraheptamolybdate tetrahydrate ( $(\text{NH}_4)_6\text{Mo}_7\text{O}_{24} \cdot 0.4 \text{H}_2\text{O}$ , 99 wt%, Alfa Aesar).

**Preparation of  $\text{Co}_3\text{Mo}_3\text{N}$ .** Firstly,  $\text{CoMoO}_4$  was prepared by dissolving the required quantities of cobalt nitrate and ammonium heptamolybdate in deionized water. The solution was then heated under reflux at  $85^\circ\text{C}$  for 12 h. The resulting purple precipitate was recovered by filtration and washed with deionized water and ethanol, followed by drying at  $100^\circ\text{C}$  overnight. The powder was then calcined at  $500^\circ\text{C}$  ( $1.5^\circ\text{C min}^{-1}$ ) for 6 h to form the desired  $\text{CoMoO}_4$  phase. After calcination, the oxide was converted to its nitride counterpart ( $\text{Co}_3\text{Mo}_3\text{N}$ ) by an ammonolysis step.

**Preparation of CoMo-N/SBA-15 catalysts.** The SBA-15 support was prepared according to the hydrothermal method, under acidic conditions as described elsewhere [26].

CoMo/SBA-15 catalysts with different loadings were prepared by an adapted impregnation-infiltration protocol. In the first step, Mo was impregnated on SBA-15 by incipient wetness impregnation under mild drying (IWI) [27]. The aqueous molybdenum precursor solution was mixed with the support and gently dried at  $25^\circ\text{C}$  for 5 days. The solid was then calcined at  $400^\circ\text{C}$  ( $1.5^\circ\text{C min}^{-1}$ ) for 5 h. At this step, SBA-15 supported  $\text{MoO}_3$  is obtained. In a second step, cobalt was added to the latter by Melt Infiltration (MI). In this method, the cobalt nitrate precursor was first ground with Mo-SBA-15 powder. The resulting solid was then transferred into a Teflon-lined autoclave and submitted to a thermal treatment at  $57^\circ\text{C}$  for 4 days. The solid was then calcined at  $500^\circ\text{C}$  ( $5^\circ\text{C min}^{-1}$ ) for 5 h.

**Ammonolysis process.** To convert the oxides into their nitrides counterpart, all the synthesized materials were subject to an ammonolysis step under  $\text{NH}_3$  (BOC, 9.98%) at a flow rate of  $60 \text{ mL min}^{-1}$  at  $785^\circ\text{C}$  for 5 h. Then, the material was cooled down to ambient temperature under ammonia flow. Upon reaching room temperature, the catalyst was purged using  $\text{N}_2$  ( $100 \text{ mL min}^{-1}$ ) for 1 h followed by a passivation step under a low concentration of oxygen gas mixture ( $99.9\% \text{ N}_2 / 0.1\% \text{ O}_2$ ) for 5 h.

**N.B.** Herein, the samples obtained after the calcination step are denoted as X-CoMo/SBA-15. The X represents the weight percentage of  $\text{CoMoO}_4$ . The catalysts obtained after the ammonolysis step are denoted as X-CoMo-N/SBA-15, while post-reaction materials are referred to as X-CoMo-N-Pr/SBA-15. The properties of SBA-15 were also studied and will

be referred to as N/SBA-15 for SBA-15 after ammonolysis, and N-Pr/SBA-15 for post-reaction material.

## 2.2. Physical and textural characterizations

**Powder X-ray diffraction (PXRD).** Wide angle PXRD patterns were collected using a Bruker X-ray AXS D8 Advance diffractometer in Bragg-Brentano geometry configuration fitted with a LynxEye Super Speed detector. XRD patterns were recorded with Cu K $\alpha$  radiation ( $\lambda = 1.54184 \text{ \AA}$ ) at 40 kV and 30 mA. Patterns are recorded over a  $2\theta$  range of  $10\text{--}80^\circ$ , at a step size of  $0.02^\circ/\text{step}$  and a counting time of  $0.5 \text{ s/step}$ . Crystal phase identification was made by comparison with the ICDD database.

**Small Angle X-ray Scattering (SAXS)** was performed on a Xeuss 2.0 (Xenocs) instrument operating under vacuum with a GeniX3D micro-source ( $\lambda = 1.54184 \text{ \AA}$ ) at  $0.6 \text{ mA}$  and  $50 \text{ kV}$  and a 2D Pilatus 3 R 200 K detector.

**Nitrogen physisorption.** Textural properties were investigated from the adsorption/desorption isotherms of  $\text{N}_2$  recorded at  $-196^\circ\text{C}$  on a Micromeritics Tristar II automated gas sorption system, operated with a software MicroActive version 4.06. Prior to the analysis, the catalysts were outgassed under dynamic vacuum at  $300^\circ\text{C}$  for 3 h. The specific surface area,  $S_{\text{BET}}$ , was calculated from the linear part of the Brunauer-Emmett-Teller plot (10 points BET Method). The total pore volume ( $V_{\text{pore}}$ ) was determined on the plateau of the adsorption branch at  $P/P_0 = 0.97$ . The pore size  $D_{\text{BJH}}$ , was evaluated using the Barret-Joyner-Halenda method applied to the adsorption branch while the micropore volume ( $V_{\text{micro}}$ ) was determined by the  $t$ -plot method.

**Solid State Nuclear Magnetic Resonance:** Samples obtained in powder form were separately packed into either 7 mm or 1.3 mm (outer diameter) rotors. All  $1\text{D } ^1\text{H}$  and  $2\text{D } ^1\text{H}\text{--}^1\text{H}$  correlation experiments were performed on a Bruker Advance NEO4 800 MHz solid-state NMR spectrometer, equipped with a 1.3 mm double-resonance magic-angle spinning (MAS) probe head with 50 kHz magic-angle spinning (MAS), operating at room temperature.  $1\text{D } ^1\text{H}$  MAS NMR spectra of all samples were acquired with 32 co-added transients.  $2\text{D } ^1\text{H}\text{--}^1\text{H}$  spin diffusion spectra were acquired with 80  $t_1$  FIDs, each with 4 co-added transients [28]. All  $^1\text{H}$  chemical shifts are calibrated with respect to neat TMS using adamantane as an external reference ( $^1\text{H}$  resonance, 1.85 ppm). All  $1\text{D } ^{29}\text{Si}$  MAS NMR experiments were performed on a Bruker Avance II 400 MHz equipped with a 7 mm double-resonance MAS probe head.

**X-ray photoelectron spectroscopy (XPS).** XPS spectra were recorded on a Kratos Analytical AXIS Ultra DLD spectrometer employing a monochromatic Al K $\alpha$  X-ray radiation (1486.6 eV), with an electron analyser operating in a fixed pass energy of 20 eV. All Binding Energies (BE) were referenced to the carbon signal corresponding to C-C bonding in the C 1 s core level at 284.8 eV. A pre-treatment chamber was used in order to mimic the catalytic pre-treatment, prior to analysis, at  $700^\circ\text{C}$  for 2 h under a  $60 \text{ mL min}^{-1}$  flow of 75 vol%  $\text{H}_2/\text{N}_2$ .

**Electron Microscopy (TEM).** Morphology analysis was performed using a TITAN Themis 300 S/TEM equipped with a high brightness Schottky field emission gun, a monochromator and a probe aberration corrector allowing energy and spatial resolution of about 150 meV and 70 pm, respectively. The microscope is equipped with several annular dark field detectors and a super-X detector system with four windowless silicon drift detectors for electron dispersive x-ray spectroscopy (EDS). The experiments have been performed at 300 kV with semi-convergence angle of about 20 mrad, probe size of the order of 500 pm and probe current between 60 and 100 pA. For high angle annular dark field (HAADF) imaging the  $c$  collection angles have been between 50 and 200 mrad. EDS mapping has been obtained in spectrum imaging mode with dwell time per pixel of about  $15 \mu\text{s}$  and continuously scanning frames until total acquisition time of about 15–20 min. All the samples were frozen at  $-120^\circ\text{C}$  in distilled water and then cut at 70 nm with an ultramicrotome equipped with a  $35^\circ$  diamond knife (Leica UCT Ultracut). Cuts were then deposited on a 200 mesh lacey carbon grid for

analysis.

**Redox properties.** The reducibility of CoMo/SBA-15 was evaluated by means of Temperature Programmed Reduction ( $\text{H}_2$ -TPR) experiment. The experiment was conducted on an Autochem chemisorption analyser (Micromeritics). Prior to the reduction, the sample (50 mg) was pre-treated under air flow ( $50 \text{ mL min}^{-1}$ ) at  $200^\circ\text{C}$  for 1 h ( $10^\circ\text{C min}^{-1}$ ) and then cooled to  $25^\circ\text{C}$ . Thereafter, temperature-programmed reduction was performed under a flow composed of 5 vol%  $\text{H}_2$  in Ar at a total flow rate of  $50 \text{ mL min}^{-1}$ . The reduction was conducted from  $25^\circ\text{C}$  to  $1000^\circ\text{C}$ , with a temperature ramp of  $5^\circ\text{C min}^{-1}$  and held for 30 min. Hydrogen consumption was recorded using a TCD detector.

**Elemental analysis.** Nitrogen analysis was undertaken using a thermo scientific FlashSmart automated elemental analyzer. The samples ( $\sim 10 \text{ mg}$ ) were weighed in tin (Sn) containers and introduced into the combustion reactor maintained at  $950^\circ\text{C}$ , promoting dynamic flash combustion of the sample. The resulting gases were quantified by a TCD detector.

**Catalytic activity:** In a typical reaction test, 0.150 g of CoMo-N/SBA-15 catalyst was placed in a quartz reactor and pre-treated at  $700^\circ\text{C}$  under a 75 vol%  $\text{H}_2/\text{N}_2$  (BOC, 99.98%) gas mixture at a total gas flow of  $60 \text{ mL min}^{-1}$  for 2 h. The reaction was then performed at  $400^\circ\text{C}$ , under the same flow rate of 75 vol%  $\text{H}_2/\text{N}_2$  for at least 10 h. Ammonia production was determined by measurement of the decrease in conductivity of a 200 mL 0.0018 M  $\text{H}_2\text{SO}_4$  solution through which the reactor effluent stream flowed and was monitored as a function of reaction time. The rate of the reaction was calculated according to the following:

$$r = \frac{\Delta_C \times n_{\text{NH}_3} \times 60}{m \times 10^{-6} \times X_{\text{wt}}}$$

Where:  $r$  is the rate of the reaction for a range of time;  $\Delta_C$  is the average change in conductivity per minute over a range of time;  $n_{\text{NH}_3}$  is the number of moles of ammonia that correspond to the decrease of  $1 \mu\text{S/cm}$ ;  $m$  is the mass of the catalyst;  $X_{\text{wt}}$  is the load wt%. The constants are added for conversion purposes to obtain the rate in  $\mu\text{mol/h.g}_{\text{active phase}}$ .

**Ammonia production under reducing condition.** Lattice nitrogen reactivity of the 10-CoMo-N/SBA-15 towards hydrogen was evaluated under reducing condition. 0.6 g of catalyst was placed in a quartz reactor and pre-treated at  $700^\circ\text{C}$  under a 75 vol%  $\text{H}_2/\text{N}_2$  (BOC, 99.98%) gas mixture at a total gas flow of  $60 \text{ mL min}^{-1}$  for 2 h. Therefore, the reactor was purged under argon and the temperature decreased at  $400^\circ\text{C}$ . The reaction was then performed at  $400^\circ\text{C}$ , under the same flow rate under a 5 vol%  $\text{H}_2/\text{Ar}$  for at least 10 h. Low  $\text{H}_2$  concentration flow was applied in order to decrease the N consumption rate from the catalyst. Quantification of ammonia was done in a similar manner to the catalytic test.

## 3. Results and discussion

### 3.1. Structural and textural properties of CoMo-N/ SBA-15

#### 3.1.1. Stability of SBA-15 under reactive conditions

**PXRD.** While the properties of SBA-15 support are extensively studied, the stability of this latter under ammonolysis conditions and under conditions relevant to ammonia synthesis is less available in the literature. In order to verify the stability of SBA-15 support through the different steps of the synthesis, SAXS patterns of the as-prepared siliceous support were first collected before and after nitridation and are presented in Fig. S1. As expected, the as-prepared siliceous support displays the characteristic three well-resolved diffraction peaks that can be associated to the (100), (110), and (200) planes of the p6mm hexagonal symmetry structure reflecting the well-defined and uniform range mesoporous structure of SBA-15 (Fig. S1-a). After the ammonolysis treatment, the support maintained its pore structure quality (Fig. S1-b) albeit a shift of the reflection peaks can be observed at higher  $2\theta$

angles from  $0.889^\circ$  to  $0.933^\circ$ . This shift indicates a slight pore contraction of the sample and could originate from the sintering occurring during the ammonolysis process ( $785^\circ\text{C}$ ). Nevertheless, as illustrated in Fig. S1-c, SBA-15 support still presents its characteristic reflections after 10 h of reaction under conditions relevant to ammonia synthesis (75 vol%  $\text{H}_2$  in  $\text{N}_2$  at a total flow rate of  $60\text{ mL min}^{-1}$ ,  $400^\circ\text{C}$ ) indicating the conservation of a good pore structure ordering within the sample.

**$\text{N}_2$  adsorption/desorption.** Complementary information on the impact of the ammonolysis treatment on the textural properties of SBA-15 was obtained through nitrogen physisorption analysis (Table 1 and Fig. S2). Before treatment, SBA-15 exhibited an adsorption/desorption isotherm of type IV with a hysteresis loop of type H1, at a relative pressure between  $P/P_0 = 0.6\text{--}0.8$ , which is typical of a mesoporous solid with highly uniform arrays of cylindrical pores with an average diameter of  $6.5\text{ nm}$  (Fig. S2-a). After ammonolysis, the study of the isotherm profile confirmed that N/SBA-15 maintained a uniform mesoporosity (Fig. S2-b). However, an important decrease of 33% in the SBA-15 accessible surface area ( $760\text{ m}^2\text{ g}^{-1}$  to  $504\text{ m}^2\text{ g}^{-1}$ ), accompanied by a decrease in pore volume ( $1.12\text{ cm}^3\text{ g}^{-1}$  to  $0.75\text{ cm}^3\text{ g}^{-1}$ ) are observed. Moreover, upon ammonolysis, N/SBA-15 was found to contain smaller pores with size centred around  $6.1\text{ nm}$  which is in line with pore contraction observed by SAXS. These changes might be related to the sintering at high temperature or to the corrosive and basic atmosphere of the ammonolysis process. However, no significant changes in the textural properties of the support were detected under ammonia synthesis reaction conditions (Fig. S2-c).

**TEM.** The morphology of the N/SBA-15 material was observed by means of HRTEM. The images (Fig. S3) show the well-ordered hexagonal arrays of the mesopores, confirming that after ammonolysis step, the characteristic porous structure of SBA-15 material is maintained as previously indicated by SAXS and  $\text{N}_2$  porosimetry results. Accumulation of nitrogen on the support is evidenced through elemental mapping. This accumulation is also confirmed by N chemical analysis through elemental analysis (CHN), which gives a N content in the material of  $\sim 2.74\text{ wt\%}$ .

**Solid-state  $^{29}\text{Si}$  and  $^1\text{H}$  NMR spectroscopy.** Fig. 1 presents 1D  $^{29}\text{Si}$  MAS NMR spectra of the as prepared SBA-15 (post-calcination), N/SBA-15 (post-ammonolysis) and N-Pr/SBA-15 (post-reaction). In the  $^{29}\text{Si}$  NMR spectrum of SBA-15, peaks at  $-90$ ,  $-100$ , and  $-110\text{ ppm}$  that can be attributed to  $\text{Si}(\text{OSi})_2(\text{OH})_2$  units ( $\text{Q}^2$ ),  $\text{Si}(\text{OSi})_3(\text{OH})$  units ( $\text{Q}^3$ ), and  $\text{Si}(\text{OSi})_4$  units ( $\text{Q}^4$ ), respectively are observed [29]. After

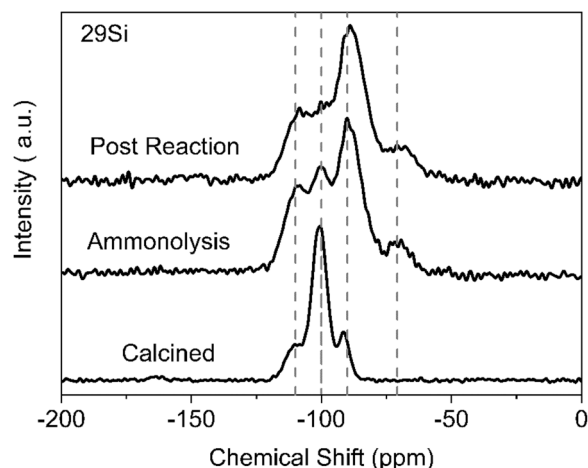


Fig. 1. Solid-state 1D  $^{29}\text{Si}$  MAS NMR spectra of (a) calcined SBA-15, (b) after ammonolysis, and (c) after 10 h of reaction.

ammonolysis, the overall line-shape of  $^{29}\text{Si}$  NMR spectrum associated with the  $\text{Q}^2$ ,  $\text{Q}^3$  and  $\text{Q}^4$  sites was retained to some degree, but slightly shifted towards high frequency values ( $\text{Q}^2$ :  $-89$ ,  $\text{Q}^3$ :  $-100$ , and  $\text{Q}^4$ :  $-109\text{ ppm}$ ). However, the relative peak intensities are different. In addition, these peaks are broader which may be related to the heterogeneity of the Si local field (non-uniform distribution of bond length and angles) after ammonolysis. More importantly, an additional strong intensity resonance at ca.  $-71\text{ ppm}$  and a weak intensity broad peak in the vicinity from  $-75\text{ ppm}$  to  $-60\text{ ppm}$  are expected to originate from the formation of surface silanol by ammonia to surface silyl-amine site ( $\text{SiO}_2\text{N}(\text{NH})_x$ ) moieties [29]. However, the extent of these surface sites is likely limited as reflected in the low intensity peak. The complete formation of an amorphous silicon nitride  $\text{Si}_3\text{N}_4$  can be safely ruled out from these results as the spectra obtained for these materials are usually characterised by large peak with maxima of  $\sim 48\text{ ppm}$ , which is not observed in the  $^{29}\text{Si}$  MAS NMR spectra [30]. Elemental analysis further corroborates NMR results and confirms the low nitrogen content in the sample  $\sim 2.74\text{ wt\%}$ . In the post-reaction SBA-15 catalyst, minor changes in  $^{29}\text{Si}$  NMR are observed as the intensity ratio of  $\text{Q}^2/\text{Q}^3$  is slightly different, with respect to the post-ammonolysis sample, which may be related to differences in silanol concentration in both samples.

Table 1

Textural properties of SBA-15, unsupported CoMo and supported CoMo-based catalysts after calcination, ammonolysis and post-reaction.

		$S_{\text{BET}}^a\text{ m}^2\cdot\text{g}^{-1}$	$S_{\mu}^b\text{ m}^2\cdot\text{g}^{-1}$	$V_p^c\text{ cm}^3\cdot\text{g}^{-1}$	$V_{\mu}^d\text{ cm}^3\cdot\text{g}^{-1}$	$D_p^e\text{ nm}$	$a_0^f\text{ nm}$	$t_0^g\text{ nm}$
CoMoO <sub>4</sub>	After calcination	6.1	–	–	–	–	–	–
	After ammonolysis	13.0	–	–	–	–	–	–
	Post-reaction	8.6	–	–	–	–	–	–
SBA-15	After calcination	760	131	1.12	0.06	6.5	11.48	4.98
	After ammonolysis	504	9.6	0.75	–	6.1	10.92	4.82
	Post-reaction	526	19.3	0.82	–	6.1	10.89	4.79
10-CoMo-N/SBA-15	After calcination	390	50	0.71	0.02	7.1	11.11	4.01
	After ammonolysis	348	19	0.71	0.005	6.8	10.87	4.07
	Post-reaction	376	–	0.65	–	6.9	11.35	4.45
20-CoMo-N/SBA-15	After calcination	344	44	0.64	0.02	7.2	10.99	3.79
	After ammonolysis	361	14.4	0.70	–	7.6	10.76	3.16
	Post-reaction	359	9.3	0.61	–	6	10.65	4.65
30-CoMo-N/SBA-15	After calcination	295	44	0.43	0.02	5.8	11.35	5.55
	After ammonolysis	285	14	0.49	–	5.8	11.11	5.31
	Post-reaction	213	4	0.35	–	5.7	11.11	5.41

<sup>a</sup>  $S_{\text{BET}}$  Calculated by the BET method;

<sup>b</sup>  $S_{\mu}$  microporous surface area;

<sup>c</sup>  $V_p$  total pore volume calculated using BJH method;

<sup>d</sup>  $V_{\mu}$  micropore volume;

<sup>e</sup>  $D_p$  mean pore size calculated using B.J.H method,

<sup>f</sup> lattice parameter calculated by hexagonal structure and bragg's equation,

<sup>g</sup> wall thickness,  $a_0 - D_p$

Furthermore, calcined, post-ammonolysis, and post-reaction SBA-15 were studied using  $^1\text{H}$ - $^1\text{H}$  2D spin diffusion (SD) NMR to characterize through-space  $^1\text{H}$ - $^1\text{H}$  proximities. In measurements of this type, magnetization is allowed to exchange between the  $^1\text{H}$  neighbouring sites using a mixing delay (as referred to as spin diffusion delay), which leads to the on- and off-diagonal peaks for chemically equivalent and inequivalent  $^1\text{H}$  sites, respectively. Fig. 2 displays 1D  $^1\text{H}$  MAS and 2D  $^1\text{H}$ - $^1\text{H}$  SD spectra of SBA-15 before and after the reaction. Prior to the ammonolysis treatment, the  $^1\text{H}$  NMR spectrum of calcined SBA-15 is mainly dominated by a major peak at  $\sim 3.8$  ppm corresponding to the surface adsorbed water, and a broad distribution of weak intensity peaks centred at 6.5 ppm and are attributable to the strong hydrogen bonding interactions between these groups and silanol protons. In the 2D  $^1\text{H}$ - $^1\text{H}$  SD spectrum of the same material (Fig. 2b), the off-diagonal peak between 3.8 ppm and 6.5 ppm indicate the through space proximity between silanol and the hydrogen bonded hydroxyl moieties. By comparison, after ammonolysis, and in the post-reaction material, the  $^1\text{H}$  peak associated with silanol groups is displaced towards high frequency values (4.5 ppm and 5.2 ppm) with this latter peak hypothesized to originate from weakly adsorbed silyl-amine sites [31–33]. In addition, a broad peak between 0 and 4 ppm appeared after ammonolysis which is likely due to the formation of silanol groups (SiOH) at different local chemical environments [32]. Further changes are observed after the post-reaction, whereby the intensities of peaks in the 0–4 ppm range (SiOH groups) are increased with respect to the water/silanol protons (4.2 ppm) which is consistent with the increased intensities of  $\text{Q}^3$  and  $\text{Q}^2$  silicon sites observed in  $^{29}\text{Si}$  NMR spectra. The increase in silanol

concentration is likely due to the reaction between  $\text{Si-O-SiO(OH)}$  and  $\text{NH}_3$  which leads to the formation of  $\text{OSiOH}$  and  $\text{H}_2\text{NSiO(OH)}$ . Additionally, subtle changes to the lineshape at 5.2 and 5.7 ppm are observed with partially resolved shoulder peaks which are expected to stem from the  $\text{NH}_3$ -like groups adsorbed on the SBA-15 [33,34]. This is further supported by the analysis of 2D SD spectra of ammonolysis and post-synthesis reaction (Fig. 2c, d) in which strong correlation peaks between the surface adsorbed water and the silyl-amine sites are observed, as depicted in the blue circles. The off-diagonal 2D peaks connecting the chemical shifts at 1.3 and 1.8 ppm and 4.5 ppm (grey boxes) are due to the close proximities between the surface adsorbed water and the silanol groups.

Overall, structural and textural properties of the SBA-15 support was indubitably impacted by the reactive conditions applied in the study. However, it was observed that N/SBA-15 maintained its ordered porous structure and satisfying surface area  $\sim 504 \text{ m}^2 \text{ g}^{-1}$ , which is still fairly high for catalytic applications. Besides, changes in the local Si environment were evidenced by  $^{29}\text{Si}$  and  $^1\text{H}$  NMR and could be attributed to the formation of silyl-amine sites ( $\text{SiO}_2\text{N}(\text{NH})_x$ ) on the silica surface. On the other hand, HRTEM and SAXS results clearly indicate that N/SBA-15 maintain the initial characteristics of a 2D hexagonally ordered structure. Thus, we demonstrate that SBA-15 is sufficiently robust under reaction conditions and is to be considered as an appropriate support for the dispersion of small metal nitride particles within its porosity.

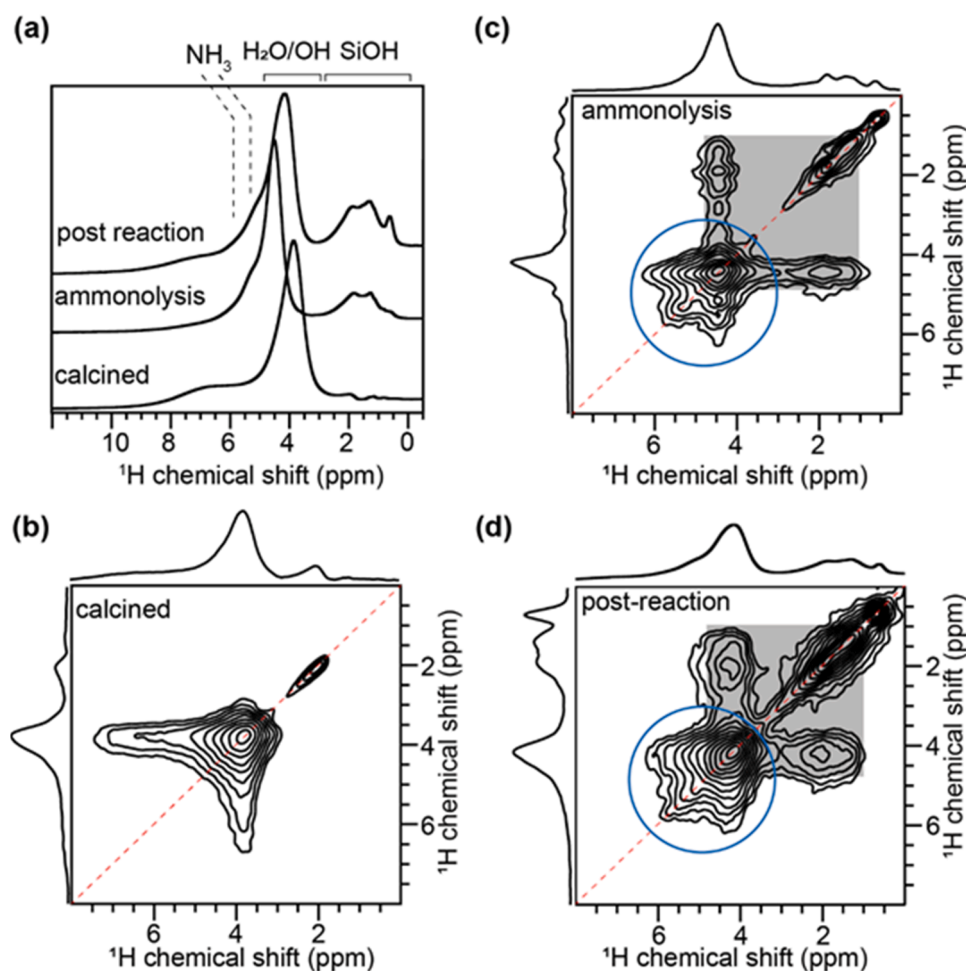


**Fig. 2.** Solid-state 1D  $^1\text{H}$  spectra of SBA-15,  $^1\text{H}$ - $^1\text{H}$  2D NMR spin diffusion spectra of (b) calcined SBA-15, (c) after ammonolysis, and (d) after 10 h of reaction. For (b-d), the spin diffusion mixing time was 500 ms. All spectra were acquired at 18.8 T (Larmor frequency of  $^1\text{H} = 800.1 \text{ MHz}$ ) with 50 kHz MAS at room temperature.

### 3.1.2. Characterization and Structural Evolution of CoMo/SBA-15 and CoMo-N/SBA-15

**PXRD. Bulk  $\text{Co}_3\text{Mo}_3\text{N}$  catalyst.** Before ammonolysis, the presence of a pure and well crystallized  $\text{CoMoO}_4$  precursor phase (PDF: 21–0868) was confirmed by PXRD (Fig. S4). The diffractogram exhibited intense and sharp PXRD diffraction peaks indicating the preparation of a well-crystallized material with a large coherent diffraction domain. Following the ammonolysis step, all the detected XRD diffraction peaks (Fig. 3) matched the  $\text{Co}_3\text{Mo}_3\text{N}$  (PDF 89–7953) confirming the formation of a pure nitride phase. As in the case of  $\text{CoMoO}_4$  intense and sharp reflections XRD peaks are observed indicating the formation of a well-crystallized nitride phase.

**CoMo/SBA-15 catalysts.** Prior to the ammonolysis step, the effective dispersion of  $\text{CoMoO}_4$  phase in SBA-15 was confirmed by PXRD in the wide-angle domain (Fig. S4) for which only poorly defined reflections of the oxide phase are observed despite loading reaching 30 wt % in the supported catalysts. Interestingly, after the ammonolysis step, no peaks related to either  $\text{Co}_3\text{Mo}_3\text{N}$  phase or single Co-N / Mo-N phases were detected on supported samples. Only a broad PXRD peak of amorphous silica was retained (Fig. 3-a). The absence of reflections related to the  $\text{Co}_3\text{Mo}_3\text{N}$  phase may be related to a possible re-dispersion of this latter during ammonolysis process. The presence of single Co-N or Mo-N phases can however not be ruled out, even if the broad signal positions below the main reflections of the  $\text{Co}_3\text{Mo}_3\text{N}$  bulk phase. SAXS

patterns collected after the ammonolysis step displayed the same diffraction patterns, with respect to the parent N/SBA-15, confirming that the derived catalysts maintained their regular pore structure through ammonolysis conditions (Fig. 3-b).

**Nitrogen adsorption-desorption analysis.** The evolution of the textural properties of the catalysts was investigated by means of  $\text{N}_2$  physisorption. The results are shown in Fig. 4, Fig. S5, and Table 1.

**Bulk  $\text{CoMoO}_4$  and  $\text{Co}_3\text{Mo}_3\text{N}$ .** The unsupported  $\text{CoMoO}_4$  and  $\text{Co}_3\text{Mo}_3\text{N}$  materials exhibited a limited accessible specific surface area (Table 1). After the ammonolysis, the surface area increased slightly from  $6.1 \text{ m}^2 \text{ g}^{-1}$  on  $\text{CoMoO}_4$  to  $13 \text{ m}^2 \text{ g}^{-1}$  on the  $\text{Co}_3\text{Mo}_3\text{N}$  counterpart. Both materials exhibited a type II isotherm reflecting their non-porous nature.

**CoMo/SBA-15.** The  $\text{N}_2$  adsorption/desorption isotherms of CoMo/SBA-15 (10, 20 and 30 wt% of CoMo) are presented in Fig. S5. 10-CoMo/SBA-15 and 20-CoMo/SBA-15 preserve a similar type IV isotherm with a hysteresis loop of type H1 with respect to the parent SBA-15. Furthermore, only a small increase in the pore size from 6.5 nm on SBA-15 to  $\sim 7.2 \text{ nm}$  on 20-CoMo/SBA-15 was observed. These results confirm that these catalysts retain the initial characteristics of SBA-15. However, the 30-CoMo/SBA-15 showed an H2b hysteresis loop, reflecting pore blocking at high CoMo loading. Compared to the SBA-15, the BET surface area of CoMo/SBA-15 catalysts showed a marked decrease with CoMo loading (from  $760 \text{ m}^2 \text{ g}^{-1}$  on SBA-15-295  $\text{m}^2 \text{ g}^{-1}$  on 30-CoMo-SBA-15 sample, see Table 1), indicating the filling of  $\text{CoMoO}_4$

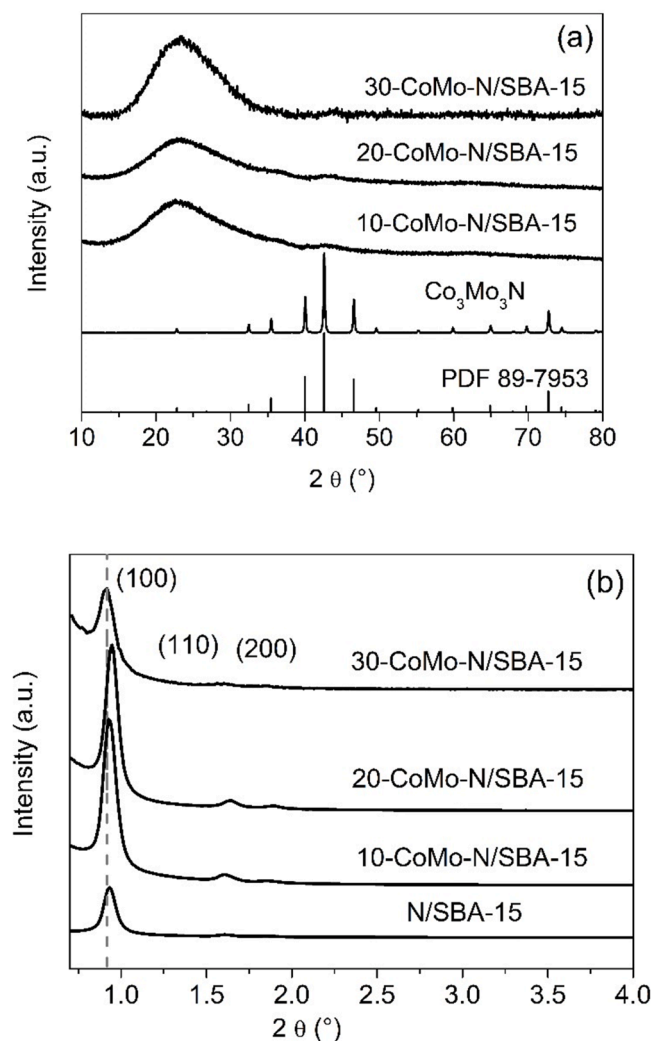


Fig. 3. PXRD patterns of  $\text{Co}_3\text{Mo}_3\text{N}$  and CoMo-N/SBA-15 with different loading. (a) wide-angle PXRD and (b) SAXS patterns.

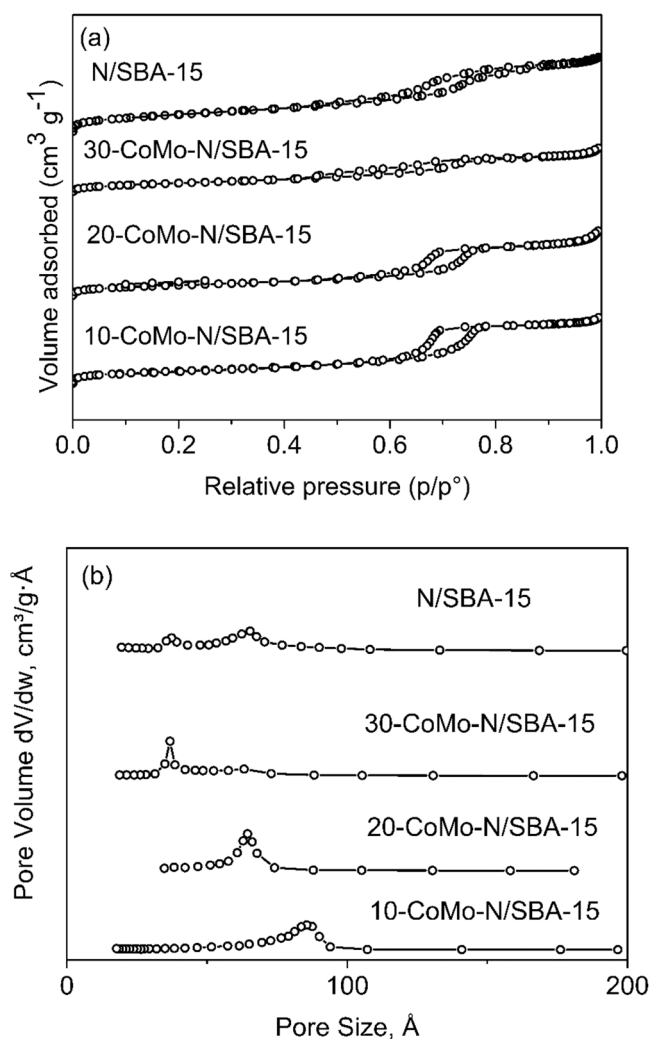


Fig. 4. (a)  $\text{N}_2$  adsorption-desorption isotherms and (b) pore size distribution of SBA-15 and CoMo-N/SBA-15 catalysts after ammonolysis.

in the channels of SBA-15.

**CoMo-N/SBA-15:** The  $N_2$  adsorption/desorption isotherms obtained after the ammonolysis step are presented in Fig. 4. The results confirm that, at low CoMo loading, the ordered mesoporous structure is mostly not altered by the ammonolysis step, while the microporous domain is strongly reduced (Table 1). Interestingly, in the CoMo-N/SBA-15, the changes, upon ammonolysis, are less significant than those observed on the bare SBA-15. In fact, only a small decrease in the accessible surface area and pore volume occurring over CoMo-N/SBA-15 is observed which might be due to the presence of nanoparticles inside SBA-15 mesoporosity.

**TEM-EDS analysis.** After ammonolysis, the morphology of CoMo-N/SBA-15 as well as the local distribution of cobalt and molybdenum species in mesoporous SBA-15 were studied by means of HAADF-STEM analysis coupled with EDS mapping. A selection of representative images of the supported samples is presented in Fig. 5 and Fig. S6.

As observed on the slice analyses ( $\sim 75$  nm thickness), the characteristic porous structure of SBA-15 material is preserved with well-

ordered mesoporous hexagonal arrays in all CoMo-N/SBA-15 which is consistent with SAXRD and  $N_2$  physisorption. Furthermore, the distribution profile of the metal species throughout the porosity of SBA-15 was observed by HAADF micrographs performed over various areas of the supported samples. As observed, nanoparticles are highly dispersed within the 2D-channels of SBA-15 for the 10-CoMo-N/SBA-15 catalyst (Fig. 5 and Fig. 6-a). Complementary EDS analysis confirm the high dispersion of Co and Mo species throughout the siliceous framework albeit some enrichment of metal species on the external surface of the grain cannot be ruled out (Fig. S6). The progressive increase of CoMo amount within the SBA-15 support could slightly amplify such external Co enrichment that is more noticeable especially on 30CoMo-N/SBA-15 (Fig. S6-c), due to the first Mo incorporation in the support that can lead to some pore entrance constriction thus limiting the infiltration of Co precursors. Therefore,  $Co_3O_4$  phase was identified by PXRD (Fig. S4) as a segregated secondary phase on the oxide material (30-CoMo/SBA-15). However, most of the Co and Mo signatures in the EDS micrographs are in close proximity, supporting the formation of CoMo-N mixed phase

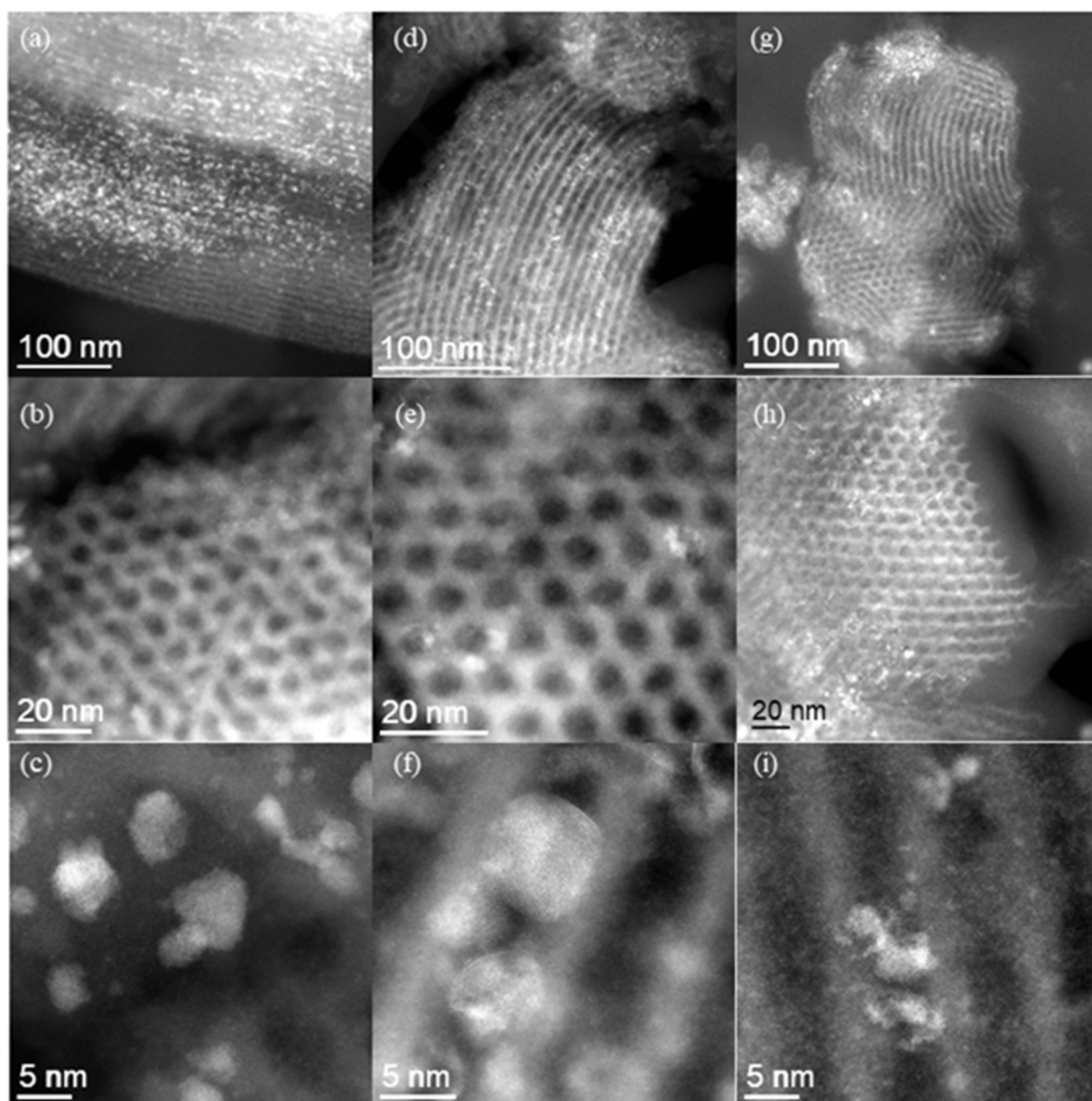


**Fig. 5.** Representative HAADF images for supported CoMo/SBA-15 after ammonolysis reaction. 10-CoMo-N/SBA-15 (a, b, and c), 20-CoMo-N/SBA-15 (d, e, and f) and 30-CoMo-N-SBA-15 (g, h, and i).

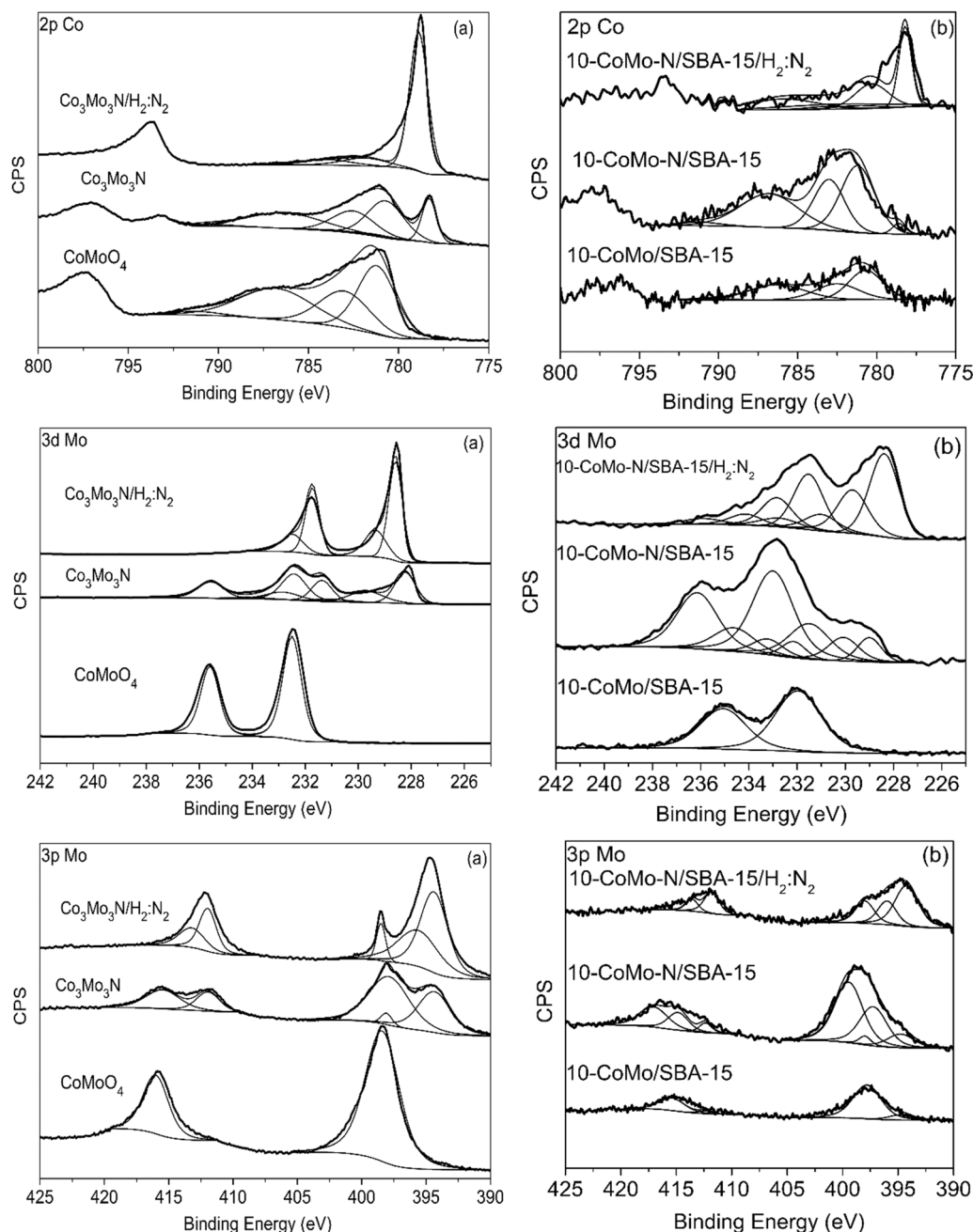


**Fig. 6.** XPS spectra in the Mo 3d region, Co 2p region and Mo 3p region of (a)  $\text{Co}_3\text{Mo}_3\text{N}$  and (b) 10-CoMo-N/SBA-15.  $\text{Co}_3\text{Mo}_3\text{N}/\text{H}_2:\text{N}_2$  and 10-CoMoN/SBA-15/ $\text{H}_2:\text{N}_2$  were subject to pre-treatment under reaction condition at 700 °C for 2 h in environmental XPS chamber before analysis.

instead of single Co-N and Mo-N phases.

**Oxidation states and chemical composition by XPS.** To gain insight into the evolution of the surface chemical composition, XPS analysis was performed for the calcined and post-ammonolysis catalysts. Furthermore, the effect of catalytic pre-treatment on the oxidation state and surface composition was also studied. The results are summarized in Fig. 6, Table S1, Table S2, and Fig. S7.

**$\text{Co}_3\text{Mo}_3\text{N}$ .** As expected, in  $\text{CoMoO}_4$ , the predominant species are  $\text{Co}^{2+}$  and  $\text{Mo}^{6+}$  (Table S1 and Table S2). However, after the ammonolysis step, Mo 3d and Co 2p XPS profiles showed a range of different oxidation states similar to those reported in the literature with the presence of Mo-O and Co-O [35]. The spectral decomposition of the high-resolution Mo 3d region can be ascribed to the  $\text{Mo}^{6+}$ ,  $\text{Mo}^{5+}$ ,  $\text{Mo}^{4+}$  and Mo-N species. The peaks characteristics of Mo-N species are of weaker intensity suggesting the formation of an oxidation layer at the

surface of  $\text{Co}_3\text{Mo}_3\text{N}$ . These results are consistent with the oxidation layer observed by HAADF-STEM (Fig. S8) which was passivated after the ammonolysis step.

In order to access the surface composition of the catalyst under reaction conditions,  $\text{Co}_3\text{Mo}_3\text{N}$  was pre-treated in an XPS environmental chamber permitting to mimic the pre-treatment used prior to the catalytic test. The use of an environmental chamber allowed us to study the surface composition of  $\text{Co}_3\text{Mo}_3\text{N}$  with minimal surface contamination. A drastic change was observed in both Mo 3d and Co 2p XPS profiles. After the pre-treatment under a flow of  $\text{H}_2/\text{N}_2$ , an important shift to lower binding energies is observed in both Co and Mo XPS profiles. These values are more aligned with the intermetallic nature of  $\text{Co}_3\text{Mo}_3\text{N}$  presenting a low valent state of metals. The high resolution of Mo 3d spectra (Fig. 6) show two major spectral lines corresponding to Mo  $3d_{5/2}$  and Mo  $3d_{3/2}$  spin-orbit components 228.59 eV and 231.73 eV of Mo-N species

[25,35]. The intensity and fraction of Mo-N is much pronounced in this case revealing the true composition of the active surface phase under reaction conditions. In the high-resolution Co 2p spectra, the position of the major spectral line was found at 778.88 eV which is in agreement with the value reported in  $\text{Co}_3\text{Mo}_3\text{N}$  prepared by Hosono's group [25]. Although this value is very close to metallic cobalt, this latter is usually reported at lower binding energy (777.9 eV).

Fig. 6 shows the spectral decomposition of high-resolution Mo 3p spectra in which N 1 s can also be observed. In this region, an intense and well resolved peak is observed at 398.4 eV which is very comparable to N 1 s observed in  $\text{Co}_3\text{Mo}_3\text{N}$  (397.9 eV) and in  $\text{Mo}_2\text{N}$  and MoN bulk (397.8 eV) [25,36]. Thus, after the pre-treatment, it can be concluded that the surface is mostly populated with N adatoms.

**CoMo-N/SBA-15:** The evolution of the surface composition of CoMo-N/SBA-15 catalysts were studied and compared to the unsupported catalyst (Fig. 6, Fig. S7, Table S1, and Table S2). In a similar manner to  $\text{CoMoO}_4$ , all the CoMo/SBA-15 obtained after calcination were composed predominantly of  $\text{Mo}^{6+}$  and  $\text{Co}^{2+}$  species. For 30-CoMo/SBA-15, an additional set of peaks were identified in the Co 2p spectra at 779.4, 780.70, 782.00, 785.00 and 789.30 eV, corresponding to  $\text{Co}_3\text{O}_4$  [37] (Fig. S7) which is in line with PXRD results. Such signals were not observed for 10-CoMo/SBA-15 sample, confirming the absence of  $\text{Co}_3\text{O}_4$  formation in this solid in agreement with PXRD results.

Upon ammonolysis, all the catalysts showed a range of oxidation states that are similar to those observed in the unsupported  $\text{Co}_3\text{Mo}_3\text{N}$ . For instance, the spectral decomposition of the high-resolution Mo 3d region showed the presence of a range of oxidation state including  $\text{Mo}^{6+}$ ,  $\text{Mo}^{5+}$ ,  $\text{Mo}^{4+}$  and Mo-N. For the 30-CoMo-N/SBA-15,  $\text{Co}_3\text{O}_4$  peaks are not observed after ammonolysis, suggesting that the latter has been successfully nitrated (Table S2). After the pre-treatment, most of the materials were composed of Mo-N and Co-N confirming that under reaction conditions, the surface is mainly populated with N adatoms. In summary, the surface composition of CoMo-N/SBA-15 was found to be very similar to the  $\text{Co}_3\text{Mo}_3\text{N}$ .

**Reducibility of CoMo/SBA-15.** The degree of interaction between the dispersed phase and SBA-15 support can be indirectly evaluated upon studying the reduction of cobalt molybdenum oxide species by  $\text{H}_2$ -TPR. The  $\text{H}_2$ -TPR results of CoMo/SBA-15 catalysts are presented in Fig. 7 and in Table S3, alongside the  $\text{CoMoO}_4$ .

The reduction temperature and  $\text{H}_2$  consumption are presented in Table S3. TPR-profile of  $\text{CoMoO}_4$  showed that the reduction process started at 600 °C. The reduction profile was characterized by two main reduction peaks at 628 and 872 °C with a smaller shoulder at 710 °C. The  $\text{H}_2$ -TPR profile agrees well with previous studies where the reduction of  $\text{CoMoO}_4$  is generally accompanied with the formation of sub-oxides intermediates such as  $\text{Co}_2\text{Mo}_3\text{O}_8$  and/or  $\text{CoMoO}_3$  [38,39].

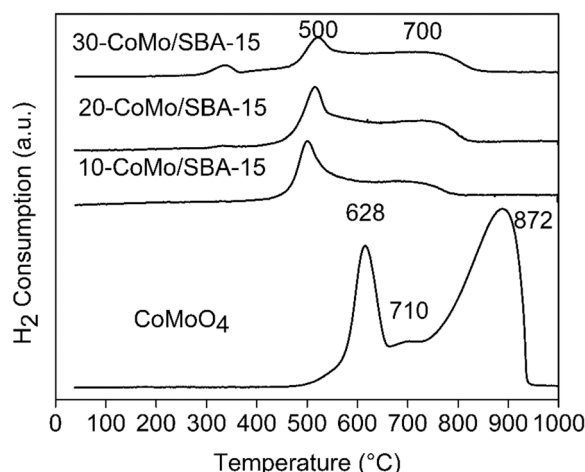


Fig. 7.  $\text{H}_2$ -TPR profiles of  $\text{CoMoO}_4$  and CoMo/SBA-15 catalysts.

Substantial changes in the reduction behaviour are observed for the CoMo/SBA-15 samples. The reduction peaks are shifted to lower temperatures, with reduction starting at temperatures as low as 450 °C. In this case, the reduction peak at lower temperature which presents higher intensity and the shoulder between both main peaks is no longer observed. Interestingly, the main reduction peak slightly shifted to higher temperatures with the increase in CoMo loading. For the 30-CoMo/SBA15 sample, an additional peak is observed at a temperature of ~ 338 °C which might be attributed to the reduction of segregated  $\text{Co}_3\text{O}_4$  phase, previously identified by PXRD analysis [40]. In summary, the reactivity of cobalt molybdates towards hydrogen was greatly improved upon dispersion on SBA-15, confirming the stabilisation of small nanoparticles within the siliceous framework.

### 3.2. Catalytic performance in ammonia synthesis

The catalytic activity of N/SBA-15 was first evaluated (Fig. 8 and Fig. 9). After 10 h of reaction, no ammonia production was measured which ruled-out the possibility of ammonia formation/desorption from the silylamine sites observed by  $^{19}\text{Si}$  and  $^1\text{H}$  NMR. Thereafter, the catalytic activity of CoMo-N/SBA-15 was studied and compared to the well-established  $\text{Co}_3\text{Mo}_3\text{N}$  catalyst.  $\text{Co}_3\text{Mo}_3\text{N}$  exhibits high catalytic activity for ammonia synthesis at ambient pressure (rate of  $248 \mu\text{mol g}_{\text{catalyst}}^{-1} \text{h}^{-1}$ , WHSV  $24\,000 \text{ mL g}^{-1} \text{h}^{-1}$ ) which is consistent with values reported in the literature but at lower WHSV  $9\,000 \text{ mL g}^{-1} \text{h}^{-1}$  [41,42]. However, it is worth noting that increasing WHSV might affect ammonia synthesis rate, and therefore a direct comparison of activity with values from the literature is difficult. Under the same catalytic testing conditions, the 10-CoMo-N/SBA-15 (rate of  $263 \mu\text{mol g}_{\text{catalyst}}^{-1} \text{h}^{-1}$ , WHSV  $24\,000 \text{ mL g}^{-1} \text{h}^{-1}$ ) exhibits close initial catalytic activity than for the  $\text{Co}_3\text{Mo}_3\text{N}$ , despite a significantly lower content of active phase in the reactor. When the active phase loading increases up to 20 wt%, almost a linear increase in the catalytic activity was observed (20-CoMo-N/SBA-15:  $479 \mu\text{mol g}_{\text{catalyst}}^{-1} \text{h}^{-1}$  WHSV  $24\,000 \text{ mL g}^{-1} \text{h}^{-1}$ ). Increasing the loading of the active phase to 30 wt%, resulted in a further increase in the catalytic activity up to  $518 \mu\text{mol g}_{\text{catalyst}}^{-1} \text{h}^{-1}$ . However, upon reaction, differences between initial catalytic activity and activity after reaching steady state conditions are observed (Table 2). The supported CoMo-N/SBA-15 displayed a stationary rate of 120, 200 and  $170 \mu\text{mol g}_{\text{catalyst}}^{-1} \text{h}^{-1}$  corresponding to the loadings of 10, 20, 30 wt% respectively. It can be seen that the stationary ammonia synthesis rate is lower than the initial rate which may denote the contribution of surface nitride decomposition by hydrogenation during the first hour of reaction. The decrease in the catalytic activity is more apparent with the 30-CoMo-N/SBA-15 which might be related to the presence of a single phase of cobalt prone to

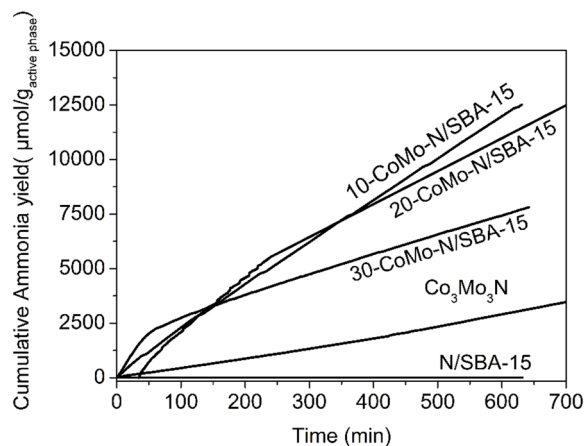
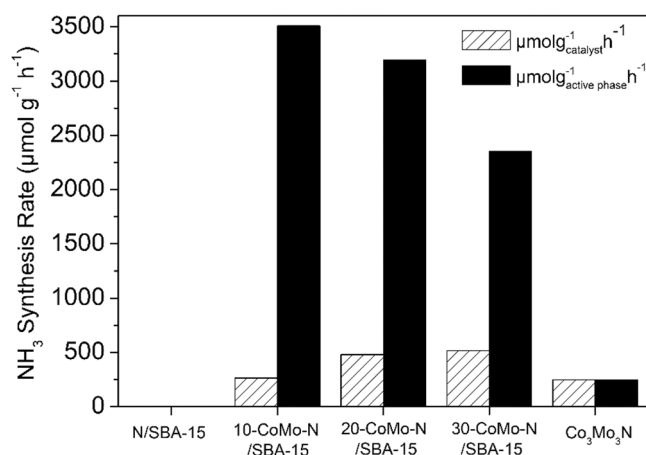


Fig. 8. Cumulative ammonia yield obtained of N-SBA-15,  $\text{Co}_3\text{Mo}_3\text{N}$ , 10-CoMo-N/SBA-15, 20-CoMo-N/SBA-15, and 30-CoMo-N/SBA-15. Reaction performed under  $60 \text{ mL min}^{-1}$  flow rate of 75 vol%  $\text{H}_2/\text{N}_2$  at 400 °C and ambient pressure.



**Fig. 9.** Initial rate of  $\text{NH}_3$  synthesis calculated for N-SBA-15,  $\text{Co}_3\text{Mo}_3\text{N}$ , 10-CoMo-N/SBA-15, 20-CoMo-N/SBA-15, and 30-CoMo-N/SBA-15. Reaction performed under 60  $\text{mL min}^{-1}$  flow rate of 75 vol%  $\text{H}_2/\text{N}_2$  at 400 °C and ambient pressure.

decomposition and deactivation.

The beneficial effect of the CoMo-N phase dispersion becomes more evident when ammonia synthesis rate is normalised with respect to the active phase loading (wt% of  $\text{Co}_3\text{Mo}_3\text{N}$  phase). For instance, at steady state conditions, a rate of  $1714 \mu\text{mol g}^{-1}_{\text{active phase}} \text{h}^{-1}$  is obtained over the 10-CoMo-N/SBA-15 catalyst. A gradual decrease is observed while increasing the cobalt molybdenum charge. Thus, the normalized ammonia synthesis rate decreased to  $1429 \mu\text{mol g}^{-1}_{\text{active phase}} \text{h}^{-1}$  and  $810 \mu\text{mol g}^{-1}_{\text{active phase}} \text{h}^{-1}$  for the 20-CoMo-N/SBA-15 and 30-CoMo-N/SBA-15 catalysts respectively. All values however remain far above the production rate registered for bulk  $\text{Co}_3\text{Mo}_3\text{N}$  ( $248 \mu\text{mol g}^{-1}_{\text{catalyst}} \text{h}^{-1}$ ). From these results, it can be concluded that the stabilization of cobalt molybdenum nitride at a nanoscale level ameliorates significantly its catalytic performance in ammonia synthesis. The progressive decrease in normalized ammonia synthesis rate with the CoMo-N loading could be linked to the pore plugging phenomenon that becomes more significant at high loading. Indeed, we observe a decrease of the normalised ammonia synthesis rate by 53% between 10% and 30% CoMo-loading. At the same time, the surface area and pore volume of the catalysts are reduced by 43% and 51% respectively. Consequently, the decrease of active phase reactivity is preferably associated to the decrease in particle accessibility inside the pores than to a reduction of the nitride phase surface/bulk reactivity.

**Thermal, textural, and structural stability of CoMo-N/SBA-15 catalysts after reaction.** The thermal stability of CoMo-N/SBA-15 catalysts is a significant challenge, especially under ammonia synthesis condition. To provide a distinct comparison between post-ammonolysis and post-reaction catalysts, a systematic study on the thermal stability of catalysts has been conducted.

**Table 2**

Summary of the catalytic activity of CoMo-N/SBA-15 catalysts in the ammonia synthesis under 60  $\text{mL min}^{-1}$  of 75%  $\text{H}_2$  in  $\text{N}_2$  (BOC, 99.98%) at 400 °C and atmospheric pressure.

	Mo/Co atomic ratio*	Initial rate		Stationary rate**	
		$\mu\text{mol g}^{-1}_{\text{catalyst}} \text{h}^{-1}$	$\mu\text{mol g}^{-1}_{\text{active phase}} \text{h}^{-1}$	$\mu\text{mol g}^{-1}_{\text{catalyst}} \text{h}^{-1}$	$\mu\text{mol g}^{-1}_{\text{active phase}} \text{h}^{-1}$
SBA-15	0	0	0	0	0
$\text{Co}_3\text{Mo}_3\text{N}$	0.99	248	248	259	259
10-CoMo-N/SBA-15	1.088	263	3507	120	1714
20-CoMo-N/SBA-15	0.796	479	3193	200	1429
30-CoMo-N/SBA-15	0.386	518	2355	170	810

\* ratio calculated from TEM/EDS quantification

\*\* Ammonia synthesis rate calculated after reaching steady state condition

Fig. 10-a shows the PXRD patterns recorded in the wide-angle domain, for the post-reaction CoMo-N/SBA-15 samples. After 10 h of reaction, no well-defined peaks related crystalline  $\text{Co}_3\text{Mo}_3\text{N}$  are detected denoting the stability of the  $\text{Co}_3\text{Mo}_3\text{N}$  phase formed under ammonia synthesis conditions. Indeed, the small broad peak observed at  $2\theta \sim 43^\circ$  might be related to the presence of nitride phase, crystallizing at the nanoscale level or that remain not crystallized. SAXS patterns collected at low angle domain shows the typical diffraction peaks related to the (100), (110), and (200) planes of the p6mm hexagonal SBA-15 symmetry structure showing that the support maintained its uniform pore structure under ammonia synthesis conditions (Fig. 10-b).

The  $\text{N}_2$  adsorption/desorption isotherms of CoMo-N-Pr/SBA-15 samples are presented in Fig. 11. After the catalytic reaction, the 10-CoMo-N-Pr/SBA-15 and 20-CoMo-N-Pr/SBA-15 catalysts maintained their isotherms of type IV with a hysteresis loop of type H1, characteristic of highly ordered structures with uniform disposition of cylindrical pore. Furthermore, only minor changes in the surface area and pore volume are observed between the post-ammonolysis and post-reaction catalyst, thus showing the good textural and structural stability of CoMo-based nitrides when supported on SBA-15. However, the 30-CoMo-N-Pr/SBA-15 showed a more pronounced surface reduction ( $285\text{--}213 \text{ m}^2 \text{g}^{-1}$ ) which might be related to structural collapse or eventually minor sintering of nitride particles occurring on external surface of silica grains.

### 3.3. Discussion

In the literature, the high catalytic activity of  $\text{Co}_3\text{Mo}_3\text{N}$  in ammonia synthesis has been correlated to the presence of active crystallographic faces that contains both Co and Mo components resulting in optimal binding energy with  $\text{N}_2$ . Initially, the role of nitrogen was believed to be limited to the creation of the appropriate surface termination planes (111). However, experimental work, enhanced by DFT-calculation, highlighted that  $\text{Co}_3\text{Mo}_3\text{N}$  might operate via the Mars-van Krevelen mechanism in which the lattice nitrogen in metal nitrides being the active species in ammonia synthesis. In this mechanism, lattice nitrogen is directly hydrogenated yielding ammonia and nitrogen lattice vacancy [43]. The nitrogen vacancy can afterwards activate molecular nitrogen to regenerate the active site. Furthermore, Zeinalipour-Yazdi et al. demonstrated via DFT computational study that  $\text{Co}_3\text{Mo}_3\text{N}$  contains a high concentration of nitrogen vacancies ( $1.6 \times 10^{16}$  to  $3.7 \times 10^{16} \text{ cm}^{-2}$ ) that can adsorb and activate  $\text{N}_2$  in conditions relevant to ammonia synthesis. Furthermore, Tsuji et al. reported enhanced catalytic activity of Co-Mo nanoparticles when supported on  $\text{CeO}_2$ . The better performance of Co-Mo/ $\text{CeO}_2$  catalyst was explained on the basis of nitrogen vacancies more easily stabilized in the Co-Mo nanoparticles than in bulky  $\text{Co}_3\text{Mo}_3\text{N}$  crystals [25]. In this context, the generation of cobalt molybdenum nanoparticles is of high interest due to its high surface area to volume ratio and the high proportion of accessible surface atoms. In the current investigation, the XPS study indicates a close surface composition of the CoMo-N/SBA-15 to  $\text{Co}_3\text{Mo}_3\text{N}$ . However, strong

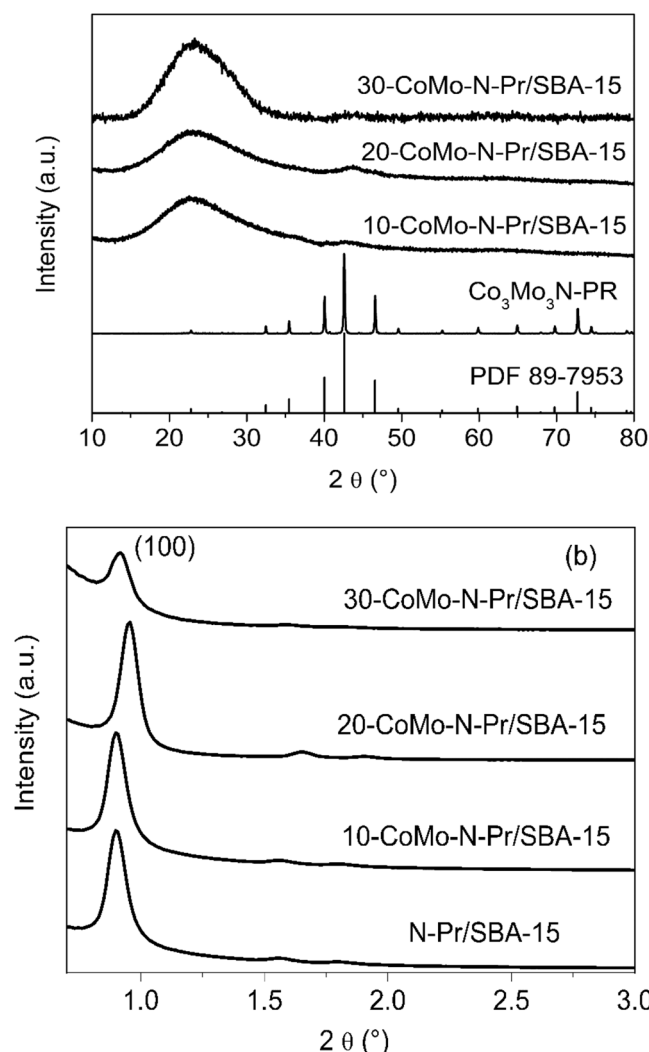


Fig. 10. PXRD patterns of post-reaction  $\text{Co}_3\text{Mo}_3\text{N-Pr}$  and CoMo-N-Pr/SBA-15. (a) wide-angle PXRD and (b) SAXS patterns.

disparities exist between  $\text{Co}_3\text{Mo}_3\text{N}$  and CoMo-N/SBA-15 in terms of structural and textural properties. For instance, all the catalysts showed high surface area with respect to the unsupported  $\text{Co}_3\text{Mo}_3\text{N}$  catalyst (up to 10 times higher). Furthermore, no XRD diffraction peaks were observed at high angle domain confirming the high dispersion of the active phase in SBA-15 structure. These findings are supported with TEM which reveals the formation of cobalt molybdenum nanoparticles stabilized within the mesopores of SBA-15. As demonstrated from the catalytic activity measurement, CoMo-N/SBA-15 displays an intrinsically high catalytic activity towards ammonia production (10-CoMo-N/SBA-15:  $1714 \mu\text{mol g}^{-1} \text{ active phase h}^{-1}$ , 20-CoMo-N/SBA-15:  $1429 \mu\text{mol g}^{-1} \text{ active phase h}^{-1}$ , and 30-CoMo-N/SBA-15:  $810 \mu\text{mol g}^{-1} \text{ active phase h}^{-1}$ ) when compared to the unsupported catalyst ( $259 \mu\text{mol g}^{-1} \text{ h}^{-1}$ ). The increase in reaction rates is seemingly consistent with the increase in accessible surface area and crystal size reduction observed by S/TEM. A parallel can be established with oxides (e.g. perovskite, hexaaluminate) operating via MvK mechanism, where previous studies, demonstrated an important increase in oxygen mobility with the decrease in crystal size leading to enhanced catalytic activities [44]. Furthermore, the mobility of lattice nitrogen and its reactivity in 10-CoMo-N/SBA-15 was confirmed under reducing conditions using  $60 \text{ mL min}^{-1}$  flow of 5 vol%  $\text{H}_2$ : Ar. Upon reaction, ammonia production in the absence of dinitrogen, was confirmed at  $400^\circ\text{C}$  (Fig. S9). Thus, the amount of ammonia produced can be directly linked to lattice

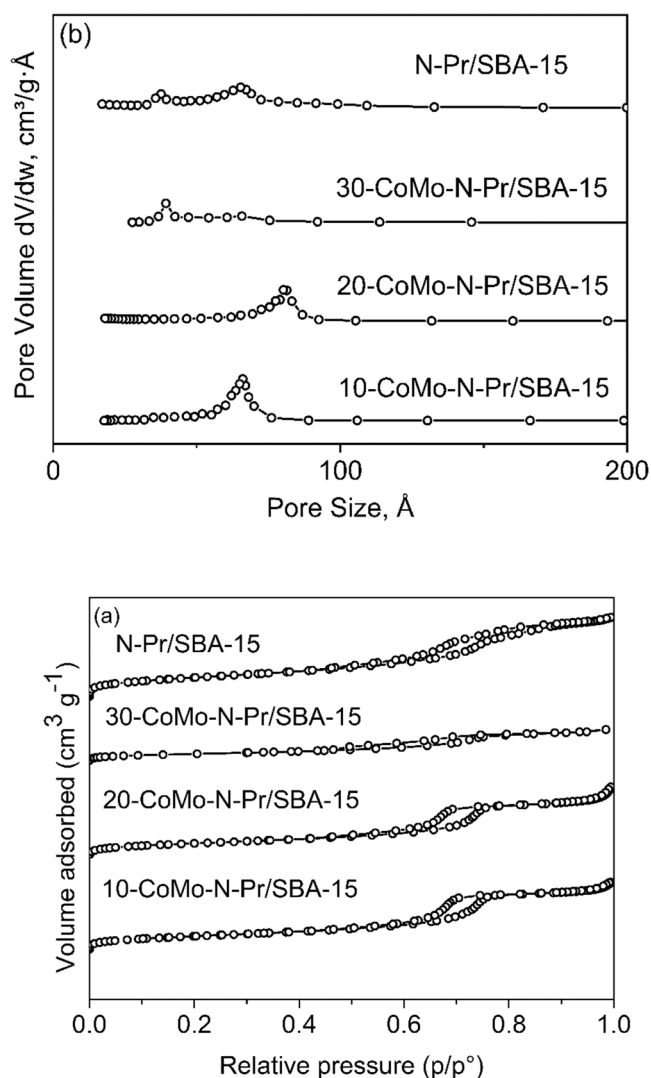


Fig. 11. (a)  $\text{N}_2$  adsorption-desorption isotherms and (b) pore size distribution of post-reaction N-Pr/SBA-15 and CoMo-N-Pr/SBA-15 catalysts.

nitrogen reacting with hydrogen. The process however, occurs in two steps, the first step suggesting the reduction of  $\text{Co}_3\text{Mo}_3\text{N}$  nanoparticle into  $\text{Co}_6\text{Mo}_6\text{N}$  as seen in the literature [45], followed by a second step transforming the reduced nitride into intermetallic phase. This mechanism is supported PXRD and HRTEM images coupled with EDS and FFT performed over post-reaction 10-CoMo-N/SBA-15 sample with evidence of formation of the intermetallic  $\text{Mo}_{6.25}\text{Co}_{6.75}$  phase (PDF number: 04-018-9512) (Fig. S10 and Table S4). The reduction process in the supported nitrides resulted in the formation of  $\text{Mo}_{6.25}\text{Co}_{6.75}$  intermetallic phase, whereas unsupported  $\text{Co}_3\text{Mo}_3\text{N}$  was only reported to reduce to the  $\text{Co}_6\text{Mo}_6\text{N}$ , which might suggest that the lattice nitrogen mobility and reactivity is crystallite size dependent. This would be consistent with the improved catalytic activity of CoMo-N/SBA-15 catalysts operating via MvK mechanism. It is also noteworthy, that beyond the improvement of nitrogen mobility in nanoparticles, given the structure-sensitivity of ammonia synthesis reaction, the performance of CoMo-N/SBA-15 could also result from an increase the high proportion of accessible surface atoms and/or increases in steps and nitrogen defects in the surface.

#### 4. Conclusion

In summary, SBA-15 was found to be a robust support for ammonia

synthesis reaction displaying good thermal and chemical stability under ammonolysis and ammonia synthesis reaction conditions. CoMo-N/SBA-15, with different loadings, was successfully prepared by two consecutive impregnation steps. The results of characterization demonstrated a high dispersion of metal nitrides within SBA-15 resulting in improved textural and structural properties. Although, changes in the local Si environment due to the formation of silyl-amine sites were evidenced by  $^{29}\text{Si}$  and  $^1\text{H}$  NMR upon ammonolysis, SBA-15 was found to be stable enough to maintain an ordered porous structure and high surface area  $\sim 504 \text{ m}^2 \text{ g}^{-1}$  for catalytic application. XPS analysis revealed that the surface composition of CoMo-N/SBA-15 catalysts is similar to the non-supported  $\text{Co}_3\text{Mo}_3\text{N}$  which is a paramount condition to develop high catalytic activity for ammonia synthesis. Because of their structural properties, i.e. a reduced crystal size and a high level of dispersion for the nitride phase, all CoMo-N/SBA-15 (10, 20 and 30 wt%) displayed enhanced catalytic activity in ammonia synthesis (1714, 1429 and  $810 \mu\text{mol g}^{-1}_{\text{active phase}} \text{ h}^{-1}$  respectively) with respect to the  $\text{Co}_3\text{Mo}_3\text{N}$  catalyst ( $259 \mu\text{mol g}^{-1}_{\text{catalyst}} \text{ h}^{-1}$ ). The lattice nitrogen mobility and reactivity towards hydrogen in the supported CoMo-N/SBA-15 was also demonstrated under reducing condition, in the absence of dinitrogen, which indicative of ammonia synthesis occurring via a mechanism similar to MvK. The enhanced catalytic activity originates probably from improving nitrogen mobility and/or alteration of the surface composition (e.g. vacancies concentrations, surface termination). The results reported in this work demonstrate that the performance of nitrides related catalyst can be greatly improved upon improving their textural and structural properties.

#### CRedit authorship contribution statement

**Amanda Sfeir:** Investigation, Formal analysis, Validation, Writing – original draft; **Camila A. Teles:** Formal analysis, Investigation. **Carmen Ciotonea:** Writing – review & editing. **G. N. Manjunatha Reddy:** Formal analysis, Investigation. **Maya Marinova:** Formal analysis, Investigation. **Jérémy Dhainaut:** Writing – review & editing. **Axel Löfberg:** Supervision, Writing – review & editing. **Jean-Philippe Dacquain:** Supervision, Conceptualization, Formal analysis, Writing – review & editing. **Sébastien Royer:** Supervision, Conceptualization, Funding acquisition, Formal analysis, Writing – review & editing. **Said Laassiri:** Supervision, Conceptualization, Funding acquisition, Formal analysis, Writing – review & editing.

#### Declaration of Competing Interest

The authors declare that they have no known competing financial interests or personal relationships that could have appeared to influence the work reported in this paper.

#### Data Availability

Data will be made available on request.

#### Acknowledgements

The authors would like to thank Mr. B. Doumert from the University of Lille for conducting NMR analyses. Thanks also goes to Pardis Simon for XPS facilities and Anne-Marie blanchenet for TEM facilities. Laassiri wishes to acknowledge the Foundation I-SITE ULNE/ France for support through the grant ERC Generator and the program MOGPA. The French national research agency is acknowledged for support via the program Make Our Planet Great Again. Chevreul Institute (FR 2638), Ministère de l'Enseignement Supérieur, de la Recherche et de l'Innovation, Région Hauts de France and FEDER are acknowledged for supporting and funding partially this work.

#### Appendix A. Supporting information

Supplementary data associated with this article can be found in the online version at doi:10.1016/j.apcatb.2022.122319.

#### References

- [1] S. Giddey, S.P.S. Badwal, C. Munnings, M. Dolan, Ammonia as a renewable energy transportation media, *ACS Sustain. Chem. Eng.* 5 (2017) 10231–10239.
- [2] A. Klerke, C.H. Christensen, J.K. Nørskov, T. Vegge, Ammonia for hydrogen storage: challenges and opportunities, *J. Mater. Chem.* 18 (2008) 2304–2310.
- [3] K.-i. Aika, L. Christiansen, I. Dybkjaer, J. Hansen, P.H. Nielsen, A. Nielsen, P. Stoltz, K. Tamaru, Ammonia: catalysis and manufacture, Springer Science & Business Media, 2012.
- [4] A. Mittasch, W. Frankenburg, Early studies of multicomponent catalysts, in: W. G. Frankenburg, V.I. Komarevsky, E.K. Rideal (Eds.), *Advances in Catalysis*, Academic Press, 1950, pp. 81–104.
- [5] I. Rafiqul, C. Weber, B. Lehmann, A. Voss, Energy efficiency improvements in ammonia production—perspectives and uncertainties, *Energy* 30 (2005) 2487–2504.
- [6] C. Smith, A.K. Hill, L. Torrente-Murciano, Current and future role of Haber–Bosch ammonia in a carbon-free energy landscape, *Energy Environ. Sci.* 13 (2020) 331–344.
- [7] L.J. Christiansen, Thermodynamic properties in ammonia synthesis, in: A. Nielsen (Ed.), *Ammonia: Catalysis and Manufacture*, Springer, Berlin Heidelberg, Berlin, Heidelberg, 1995, pp. 1–15.
- [8] J. Humphreys, R. Lan, S. Tao, Development and recent progress on ammonia synthesis catalysts for haber–bosch process, *advanced energy and sustainability, Research* 2 (2021) 2000043.
- [9] R. Kojima, K.-i. Aika, Cobalt molybdenum bimetallic nitride catalysts for ammonia synthesis, *Chem. Lett.* 29 (2000) 514–515.
- [10] C.J.H. Jacobsen, Novel class of ammonia synthesis catalysts, *Chem. Commun.* (2000) 1057–1058.
- [11] C.J.H. Jacobsen, S. Dahl, B.S. Clausen, S. Bahn, A. Logadottir, J.K. Nørskov, Catalyst design by interpolation in the periodic table: bimetallic ammonia synthesis catalysts, *J. Am. Chem. Soc.* 123 (2001) 8404–8405.
- [12] C.D. Zeinalipour-Yazdi, J.S.J. Hargreaves, C.R.A. Catlow, Nitrogen activation in a mars–van krevelen mechanism for ammonia synthesis on  $\text{Co}_3\text{Mo}_3\text{N}$ , *J. Phys. Chem. C* 119 (2015) 28368–28376.
- [13] S.M. Hunter, D.H. Gregory, J.S.J. Hargreaves, M. Richard, D. Duprez, N. Bion, A study of  $^{15}\text{N}/^{14}\text{N}$  isotopic exchange over cobalt molybdenum nitrides, *ACS Catal.* 3 (2013) 1719–1725.
- [14] A. Daisley, L. Costley-Wood, J.S.J. Hargreaves, The role of composition and phase upon the lattice nitrogen reactivity of ternary molybdenum nitrides, *Top. Catal.* 64 (2021) 1021–1029.
- [15] C.D. Zeinalipour-Yazdi, J.S.J. Hargreaves, S. Laassiri, C.R.A. Catlow, The integration of experiment and computational modelling in heterogeneously catalysed ammonia synthesis over metal nitrides, *Phys. Chem. Chem. Phys.* 20 (2018) 21803–21808.
- [16] S. Laassiri, C.D. Zeinalipour-Yazdi, C.R.A. Catlow, J.S.J. Hargreaves, Nitrogen transfer properties in tantalum nitride based materials, *Catal. Today* 286 (2017) 147–154.
- [17] X. Wang, M. Su, H. Zhao, Process design and exergy cost analysis of a chemical looping ammonia generation system using  $\text{AlN}/\text{Al}_2\text{O}_3$  as a nitrogen carrier, *Energy* 230 (2021), 120767.
- [18] R. Michalsky, A.M. Avram, B.A. Peterson, P.H. Pfromm, A.A. Peterson, Chemical looping of metal nitride catalysts: low-pressure ammonia synthesis for energy storage, *Chem. Sci.* 6 (2015) 3965–3974.
- [19] M.E. Gálvez, M. Halmann, A. Steinfeld, Ammonia production via a two-step  $\text{Al}_2\text{O}_3/\text{AlN}$  thermochemical cycle. 1. Thermodynamic, environmental, and economic analyses, *Ind. Eng. Chem. Res.* 46 (2007) 2042–2046.
- [20] R. Michalsky, P.H. Pfromm, A. Steinfeld, Rational design of metal nitride redox materials for solar-driven ammonia synthesis, *Interface Focus* 5 (2015) 20140084.
- [21] S. Laassiri, N. Bion, D. Duprez, H. Alamdari, S. Royer, Role of  $\text{Mn}^{+}$  cations in the redox and oxygen transfer properties of  $\text{BaMxAl}_{12-x}\text{O}_{19-\delta}$  ( $\text{M} = \text{Mn, Fe, Co}$ ) nanomaterials for high temperature methane oxidation, *Catal. Sci. Technol.* 3 (2013) 2259–2269.
- [22] S. Laassiri, C.D. Zeinalipour-Yazdi, N. Bion, C.R.A. Catlow, J.S.J. Hargreaves, Combination of theoretical and in situ experimental investigations of the role of lithium dopant in manganese nitride: a two-stage reagent for ammonia synthesis, *Faraday Discuss.* 229 (2021) 281–296.
- [23] I.B. Parker, K.C. Waugh, M. Bowker, On the structure sensitivity of ammonia synthesis on promoted and unpromoted iron, *J. Catal.* 114 (1988) 457–459.
- [24] Z. Song, T. Cai, J.C. Hanson, J.A. Rodriguez, J. Hrbek, Structure and reactivity of Ru nanoparticles supported on modified graphite surfaces: a study of the model catalysts for ammonia synthesis, *J. Am. Chem. Soc.* 126 (2004) 8576–8584.
- [25] Y. Tsuji, K. Ogasawara, M. Kitano, K. Kishida, H. Abe, Y. Niwa, T. Yokoyama, M. Hara, H. Hosono, Control of nitrogen activation ability by Co–Mo bimetallic nanoparticle catalysts prepared via sodium naphthalenide-reduction, *J. Catal.* 364 (2018) 31–39.
- [26] H. Lin, X. Zhong, C. Ciotonea, X. Fan, X. Mao, Y. Li, B. Deng, H. Zhang, S. Royer, Efficient degradation of clofibric acid by electro-enhanced peroxydisulfate activation with Fe–Cu/SBA-15 catalyst, *Appl. Catal. B Environ.* 230 (2018) 1–10.

- [27] A. Ungureanu, B. Dragoi, A. Chiriac, C. Ciotonea, S. Royer, D.A. Duprez, A. S. Mamede, E. Dumitriu, Composition-dependent morphostructural properties of Ni-Cu oxide nanoparticles confined within the channels of ordered mesoporous SBA-15 silica, *ACS Appl. Mater. Interfaces* 5 (8) (2013) 3010–3025.
- [28] P. Raval, J. Trébosc, T. Pawlak, Y. Nishiyama, S.P. Brown, G.N. Manjunatha Reddy, Combining heteronuclear correlation NMR with spin-diffusion to detect relayed Cl–H–H and N–H–H proximities in molecular solids, *Solid State Nucl. Magn. Reson.* 120 (2022), 101808.
- [29] B. Singh, K.R. Mote, C.S. Gopinath, P.K. Madhu, V. Polshettiwar, SBA-15-oxynitrides as a solid-base catalyst: effect of nitridation temperature on catalytic activity, *Angew. Chem. Int. Ed.* 54 (2015) 5985–5989.
- [30] P.M. Rewatkar, T. Taghvaei, A.M. Saeed, S. Donthula, C. Mandal, N. Chandrasekaran, T. Leventis, T.K. Shruthi, C. Sotiriou-Leventis, N. Leventis, Sturdy, monolithic SiC and Si<sub>3</sub>N<sub>4</sub> aerogels from compressed polymer-cross-linked silica xerogel powders, *Chem. Mater.* 30 (2018) 1635–1647.
- [31] T. Asefa, M. Kruk, N. Coombs, H. Grondy, M.J. MacLachlan, M. Jaroniec, G. A. Ozin, Novel route to periodic mesoporous aminosilicas, PMAs: ammonolysis of periodic mesoporous organosilicas, *J. Am. Chem. Soc.* 125 (2003) 11662–11673.
- [32] B. Grünberg, T. Emmeler, E. Gedat, I. Shenderovich, G.H. Findenegg, H.-H. Limbach, G. Buntkowsky, Hydrogen bonding of water confined in mesoporous silica MCM-41 and SBA-15 studied by <sup>1</sup>H solid-state NMR, *Chem. A Eur. J.* 10 (2004) 5689–5696.
- [33] S. Lang, M. Benz, U. Obenaus, R. Himmelmann, M. Scheibe, E. Klemm, J. Weitkamp, M. Hunger, Mechanisms of the AlCl<sub>3</sub> modification of siliceous microporous and mesoporous catalysts investigated by multi-nuclear solid-state NMR, *Top. Catal.* 60 (2017) 1537–1553.
- [34] Z. Li, C. Rieg, A.-K. Beurer, M. Benz, J. Bender, C. Schneck, Y. Traa, M. Dyballa, M. Hunger, Effect of aluminum and sodium on the sorption of water and methanol in microporous MFI-type zeolites and mesoporous SBA-15 materials, *Adsorption* 27 (2021) 49–68.
- [35] Y. Sun, L. Wang, O. Guselnikova, O. Semyonov, J. Fraser, Y. Zhou, N. López, A. Y. Ganin, Revealing the activity of Co<sub>3</sub>Mo<sub>3</sub>N and Co<sub>3</sub>Mo<sub>3</sub>N<sub>0.5</sub> as electrocatalysts for the hydrogen evolution reaction, *J. Mater. Chem. A* 10 (2022) 855–861.
- [36] L. Wang, S. Zhao, Y. Liu, D. Liu, J.M. Razal, W. Lei, Interfacial engineering of 3D hollow Mo-based carbide/nitride nanostructures, *ACS Appl. Mater. Interfaces* 13 (2021) 50524–50530.
- [37] M.C. Biesinger, B.P. Payne, A.P. Grosvenor, L.W.M. Lau, A.R. Gerson, R.S.C. Smart, Resolving surface chemical states in XPS analysis of first row transition metals, oxides and hydroxides: Cr, Mn, Fe, Co and Ni, *Appl. Surf. Sci.* 257 (2011) 2717–2730.
- [38] J.A. Rodriguez, S. Chaturvedi, J.C. Hanson, J.L. Brito, Reaction of H<sub>2</sub> and H<sub>2</sub>S with CoMoO<sub>4</sub> and NiMoO<sub>4</sub>: TPR, XANES, time-resolved XRD, and molecular-orbital studies, *J. Phys. Chem. B* 103 (1999) 770–781.
- [39] J.A. Rodriguez, J.Y. Kim, J.C. Hanson, J.L. Brito, Reduction of CoMoO<sub>4</sub> and NiMoO<sub>4</sub>: in situ time-resolved XRD studies, *Catal. Lett.* 82 (2002) 103–109.
- [40] E. Van Steen, G.S. Sewell, R.A. Makhoe, C. Micklethwaite, H. Manstein, M. De Lange, C.T. O'Connor, TPR study on the preparation of impregnated Co/SiO<sub>2</sub> catalysts, *J. Catal.* 162 (1996) 220–229.
- [41] R. Kojima, K.-i. Aika, Cobalt molybdenum bimetallic nitride catalysts for ammonia synthesis: part 1. Preparation and characterization, *Appl. Catal. A: Gen.* 215 (2001) 149–160.
- [42] J.S.J. Hargreaves, D. McKay, A comparison of the reactivity of lattice nitrogen in Co<sub>3</sub>Mo<sub>3</sub>N and Ni<sub>2</sub>Mo<sub>3</sub>N catalysts, *J. Mol. Catal. A: Chem.* 305 (2009) 125–129.
- [43] T.-N. Ye, S.-W. Park, Y. Lu, J. Li, M. Sasase, M. Kitano, H. Hosono, Contribution of nitrogen vacancies to ammonia synthesis over metal nitride catalysts, *J. Am. Chem. Soc.* 142 (2020) 14374–14383.
- [44] S. Laassiri, N. Bion, D. Duprez, S. Royer, H. Alamdari, Clear microstructure–performance relationships in Mn-containing perovskite and hexaaluminate compounds prepared by activated reactive synthesis, *Phys. Chem. Chem. Phys.* 16 (2014) 4050–4060.
- [45] S.M. Hunter, D. McKay, R.I. Smith, J.S.J. Hargreaves, D.H. Gregory, Topotactic nitrogen transfer: structural transformation in cobalt molybdenum nitrides, *Chem. Mater.* 22 (2010) 2898–2907.